

Enhanced Extraction Rates through Gap States of Molybdenum Oxide Anode Buffer

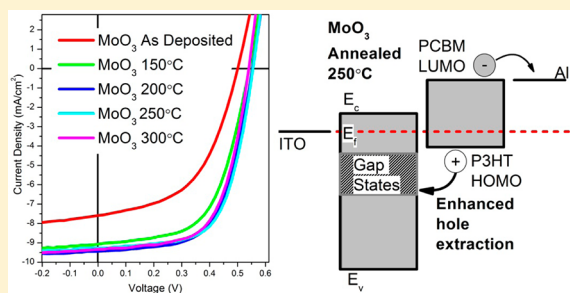
Binayak Dasgupta,[†] Wei Peng Goh,[†] Zi En Ooi,[†] Lai Mun Wong,[†] Chang Yun Jiang,[†] Yi Ren,[†] Eng Soon Tok,[‡] Jisheng Pan,[†] Jie Zhang,^{*,†} and Sing Yang Chiam^{*,†}

[†]Institute of Materials Research and Engineering, A*STAR (Agency for Science, Technology and Research), 3 Research Link, Singapore 117602

[‡]Department of Physics, National University of Singapore, 2 Science Drive 3, Singapore 117542

S Supporting Information

ABSTRACT: Molybdenum oxide (MoO_3) is a promising anode buffer layer (ABL) for high-performance organic photovoltaic (OPV) devices. However, the reasons for the enhanced performances remain unclear. In this work, we show that defect states play an important, if not dominating, role in improving the OPV performances. The changes in both the density of defect states and the work function of MoO_3 with annealing are shown and correlated with the OPV device performance. The increased defect densities improve the OPV performance through an enhanced hole extraction rate at the MoO_3 /organic interface. The reduction in work function, however, reduces the interface field that can possibly lower mobility near the interface and reduce the electron-blocking effect. This plays a role in saturation of the device performance. This work, therefore, shows the importance of the defects in MoO_3 as an ABL and a dominance of defect-enhanced extraction over a field-enhanced extraction process.



1. INTRODUCTION

Organic photovoltaic (OPV) cells provide advantages, such as lower fabrication costs, better portability, and flexibility, over conventional solar cells.^{1–4} The bulk heterojunction (BHJ) OPV structure is commonly used due to its proven performances.^{5,6} In general, the BHJ OPV structure consists of a photoactive donor–acceptor polymer blend sandwich between anodes and cathodes. While the maximum achievable power conversion efficiency (PCE) of the OPV is intrinsically limited by the photoactive donor–acceptor polymer blend, optimization of the anode and cathode buffer layers play a critical role in achieving the maximum performances.^{7–9} Poly(3,4-ethylenedioxythiophene) poly(styrenesulfonate) (PEDOT:PSS) is a hole-transport material that is commonly used as the anode buffer layer (ABL) because of its good contact properties with the donor polymer and the transparent conductor.^{7,10} However, corrosion from its high acidity means that the device reliability is affected and there is a need to find suitable substitutes.^{4,11} A promising class of materials are the transition-metal oxides, such as MoO_3 , NiO , V_2O_5 , and WO_3 , and these materials have demonstrated promising potential to act as effective ABLs.^{12–14}

In particular, MoO_3 has attracted considerable interest, and several studies have already demonstrated its feasibility by showing similar or even better OPV performance when compared to the use of PEDOT:PSS as an ABL.^{13,15–20} However, a coherent understanding of MoO_3 as a hole extraction layer is still lacking. One possible reason for the lack of clarity partly arises from the varying reported values of work

function and ionization potential of MoO_3 since this adds to the difficulty in understanding the charge extractions.^{21–23} In addition, while MoO_3 with oxygen defects is an intrinsic n-type material, reports have shown that MoO_3 can enhance the extraction and injection of both electrons and holes at the interface.^{24–27} It is, therefore, not intuitive how an n-type oxide can act as an efficient hole injection, extraction, and transport layer. To explain the efficient hole extraction and transport, reports initially assumed MoO_3 to possibly be a p-type material. This was subsequently replaced by the explanation of an improved extraction through a more favorable alignment of the valence band of MoO_3 with the organic materials.^{12,28–32} However, this explanation was called into question when MoO_3 was shown to have a much higher work function and ionization potential than previously assumed.^{21–23,33} The high work function of MoO_3 is now believed to result in a significant shift in the vacuum level that enhanced band bending at the MoO_3 /organic interface such that it favors hole extraction, especially in OPVs. This has been reported for both organic small molecules^{16,34} and polymers.³⁵ The enhanced hole extraction from the active layers to the anode resulted in a reduced series resistance, better fill factor, and thus better performance. In addition, MoO_3 has intrinsic oxygen vacancy defects that appear as filled states in the forbidden energy gap.^{36–38} These

Received: November 19, 2012

Revised: January 2, 2013

Published: March 26, 2013

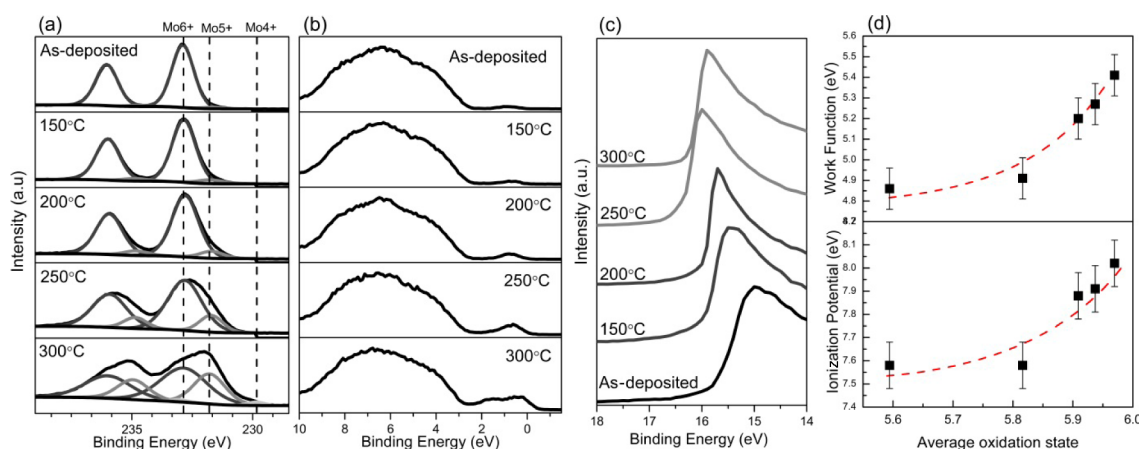


Figure 1. Photoelectron characterization of MoO₃ films annealed in a N₂ environment: (a) Mo 3d XPS spectra with the components from Mo 6+, 5+, and 4+ indicated; (b) valence scans of MoO₃ showing the increase in the oxygen vacancy gap states. (c) UPS secondary-electron cutoff valence spectra. (d) Plot of work function and ionization potential against average Mo oxidation state in the MoO₃ film.

defects have also been suggested to enhance the hole injection in organic light-emitting diodes^{24–26} and hole extraction in both organic^{20,34,38} and inorganic solar cells.³⁹ In this case, it is proposed that these gap states provided additional pathways for the enhancement of hole injection or extraction.^{40,41} Therefore, it is important to better understand the different reasons for the enhancement in using MoO₃ in OPV devices. Recent work shows the lowering of the MoO₃ work function with the increasing presence of oxygen vacancies.²³ This presents an ideal case to investigate the explanations of field-enhanced extraction and/or defects-enhanced extraction at the MoO₃/organic interface.

In this paper, we investigate the OPV device performances of identical cells with MoO₃ thin films that contain different defect concentrations. This is analyzed together with changes in work function and ionization potential since this can potentially affect the energy alignment and hence band bending at the interface. Generation of oxygen vacancy gap states in the MoO₃ thin films is achieved by annealing at various temperatures in oxygen-deficient nitrogen environments. OPV devices are fabricated in parallel with photoelectron spectroscopy measurements for the different MoO₃ films used as ABLs in BHJ OPV devices.

2. EXPERIMENTAL DETAILS

Indium tin oxide (ITO)-coated glass from Merck Co. was used as substrates. These were precleaned in an ultrasonic bath with several solvents, to remove surface contaminants. MoO₃ thin films were thermally evaporated in a chamber with a base pressure of approximately 2×10^{-6} mbar. Because the thicknesses can affect the OPV performance, the rate of deposition was kept at a value of 1.2 nm/min as monitored using a quartz microbalance. In this work, we have investigated MoO₃ thicknesses of both 5 and 10 nm oxides, but we will only report the 5 nm results since they are similar (Supporting Information, S1). The deposited MoO₃ films were then annealed on a hot plate, in a nitrogen glovebox environment, at different temperatures for 10 min to generate the oxygen vacancy defects. The annealed films were then transferred from the glovebox into an ultra-high-vacuum (10^{-10} mbar) VG ESCALAB 220i-XL photoemission spectroscopy system equipped with a monochromatic Al K α (1486.6 eV) X-ray and ultraviolet gas discharge lamp as excitation sources. The electron analyzer was calibrated with polycrystalline gold, silver,

and copper (polycrystalline) standard samples by setting the Au 4f_{7/2}, Ag 3d_{5/2}, and Cu 2p_{3/2} peaks at binding energies of 84.0 ± 0.05 , 368.25 ± 0.05 , and 932.65 ± 0.05 eV. The Fermi edge was calibrated with a polycrystalline Ni sample. The measurement resolution from this calibration is better than 0.1 eV. The high-energy resolution scans were recorded with a pass energy of 20 eV, and scans where applicable were carbon corrected to the binding energy of 284.6 ± 0.1 eV. The unfiltered He I (21.22 eV) photons were used for work function measurements, and the secondary cutoff was obtained under an applied bias of -15 V.⁴² The transfer to the characterization chamber was completed with a controlled air exposure duration of ~ 20 min.

The same batch of deposited and subsequent annealed MoO₃ films was used for the fabrication of OPV devices with the structure ITO/MoO₃/P3HT:PCBM/Al. The annealed MoO₃ films were also subjected to the controlled air exposure for ~ 20 min to enable meaningful comparisons with the separately characterized films. In addition, control experiments were carried out to fabricate OPV with ABLs that are not exposed, and the 20 min exposure step did not degrade the device performance (Supporting Information, S2). The active layer is a mixed solution of regioregular poly(3-hexylthiophene) (P3HT, from Sigma-Aldrich) and 6,6-phenyl-C61-butyric acid methylester (PCBM, from Nano-C) with a weight ratio of 5:4 in dichlorobenzene solvent that was then spin-coated onto the MoO₃ layer and annealed at 120 °C for 10 min. This was dried for 2 h before a 100 nm Al cathode was evaporated onto the active layer through a shadow mask at a rate of ~ 0.1 nm/s. Control devices were fabricated using poly(3,4-ethylenedioxythiophene) poly(styrenesulfonate) (PEDOT:PSS) as ABLs, spin-coated onto the cleaned patterned ITO-coated substrates in ambient conditions while the rest of the fabrication process was identical. The current–voltage (I–V) measurements were carried out with a Keithley 2400 Sourcemeter in the dark and under 100 mW/cm² (AM 1.5G) illumination using a 16S-002 (Solar Light Company Inc.) solar simulator.

3. RESULTS AND DISCUSSION

A. Defect Generation and Work Function Changes in Annealed MoO₃ Films. The presence and density of the filled defect gap states can be measured using photoelectron spectroscopy. Figure 1a,b shows the XPS measured Mo 3d and valence spectra, respectively, of MoO₃ films after annealing

in a reducing ambient at the indicated temperatures. The Mo 3d spectra were carefully fitted with contributions from +6, +5, and +4 oxidation states at 232.7, 231.2, and 229.5 eV, respectively, for the 3d_{5/2} spin-orbit split peak.^{23,43–46} The deviation from a +6 oxidation state can be attributed to the formation of defect states arising from oxygen vacancies. When MoO₃ films are annealed in temperatures that are less than 250 °C, only the Mo⁵⁺ defect states are observed in the XPS scans. At the same time, a density of occupied gap states arises in the range of 0.4–1.2 eV below the Fermi level (Figure 1b). However, at a higher annealing temperature of 300 °C, the formation of Mo⁵⁺ states is clearly observed along with a small contribution from the Mo⁴⁺ oxidation states. There is also an increase in the defect bandwidth with a characteristic splitting attributed to the formation of ordered defects in the metallic MoO₂.^{47,48} Our studies reveal that progressive annealing of MoO₃ up to 250 °C results in the formation of lower oxidation Mo and the occupation of defect states near the Fermi level, while the formation of metallic MoO₂ starts to occur at higher annealing temperatures. The above observations are in agreement with the recent literature.^{23,47–49}

The changes in the work function of the annealed MoO₃ films were also measured using UPS. Figure 1c shows the secondary cutoff spectra of as-deposited MoO₃ layers annealed at different temperatures as indicated. There was a reduction in the work function shown by a shift of the secondary cutoff in Figure 1c toward a higher binding energy when the film was annealed at 150 °C. The changing work function then appears to stabilize at higher annealing temperatures. We also highlight here that, upon ambient exposure, we found that adsorption of nitrogen on the surface occurs spontaneously (Supporting Information, S3) and these adsorptions, which are overlooked previously, can affect the measured work function values of the MoO₃. Recently, Greiner et al. showed the correlation between work function and oxidation states.²³ Therefore, we examine our measured work function and ionization potential values with the fitted average Mo oxidation states in the as-deposited and annealed MoO₃ film, as shown in Figure 1d. The average Mo oxidation state was estimated from the atomic percentages derived from the fitted Mo 3d core-level spectra. Similar to the trend proposed by Greiner et al.,²³ it is observed that the work function and ionization potential of MoO₃ are reduced when the oxidation state is less than the stoichiometry value of 6. The creation of filled defect states from oxygen defects, therefore, resulted in an increase of surface electron doping. The opposing trends of an increase in defect densities and a reduction in work function can now be studied in terms of their effects on the OPV device performances.

B. Improvement in OPV Device Performance: Enhancement of Extraction Rate. The characterization of the defect densities was done in parallel with the OPV device fabrication. The same batches of deposited MoO₃, with the same exposure durations, were used for both the characterization and OPV device fabrication. The current–voltage characteristics of the OPV devices shown in Figure 2 can, therefore, be compared against the varying defects and work function of MoO₃ with annealing. The average OPV performances, including the efficiencies, are summarized in Table 1. Annealing of the anode buffer layer leads to a substantial improvement in the overall cell performance, and this is clearly reflected in Figure 2a that shows the OPV performance under AM 1.5 illumination. The improvements are more pronounced when comparing between as-deposited and annealed films with

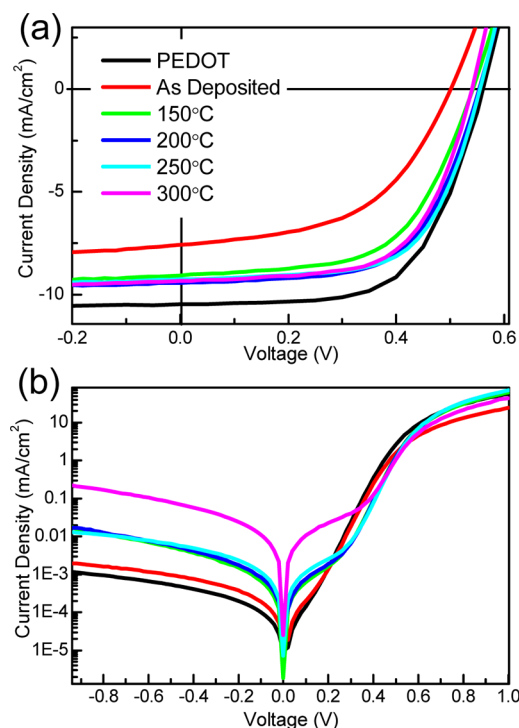


Figure 2. (a) Current–voltage characteristics of OPV devices with different ABLs: PEDOT control, and MoO₃ as-deposited and annealed at the indicated temperatures, under 100 mW/cm² (AM 1.5G) illumination. (b) Semilogarithm plot of dark current–voltage characteristics of OPV devices with different ABLs: PEDOT control, and MoO₃ as-deposited and annealed at the indicated temperatures.

Table 1. Summary of OPV Parameters for the Devices with Different ABLs: PEDOT Control, and MoO₃ As-Deposited and Annealed at the Indicated Temperatures

device	V_{oc} (V)	J_{sc} (mA/cm ²)	fill factor	PCE (%)	R_s (Ω·cm ²)	R_p (Ω·cm ²)
PEDOT	0.56	−10.5	0.62	3.7	9.5	2000.0
as-deposited	0.50	−7.6	0.51	2.0	16.9	461.5
150 °C	0.54	−9.1	0.59	2.9	13.1	631.6
200 °C	0.55	−9.4	0.62	3.2	10.6	1285.7
250 °C	0.56	−9.3	0.64	3.3	9.6	1799.9
300 °C	0.54	−9.3	0.62	3.1	8.5	1125.0

only slight improvements when the annealing temperature is increased from 200 to 250 °C. The short-circuit current (J_{sc}) and open-circuit voltage (V_{oc}) values, shown in Table 1, improved in the devices with annealed MoO₃ ABLs. The highest V_{oc} is attained for the MoO₃ annealed at 250 °C, and this value is similar (within ~1%) to the control PEDOT device. The series (R_s) and parallel (R_p) resistance in Table 1 show a systematic improvement with the increasing annealing temperature, resulting in a higher fill factor (FF). The power conversion efficiency (PCE) of 3.3% for MoO₃ ABL annealed at 250 °C is comparable with available reports that utilize similar material and architectures.⁵⁰

Because only modifications were made to the anode buffer layer, the improvements can be discussed by examining the MoO₃/organic interface. Generally, the observed OPV device parameter improvements can be attributed to an increase in the hole extraction rate at the anode contact upon annealing. The most immediate indication of a higher extraction rate is the reduction in R_s . The dark current shown in Figure 2b shows an

increase in the magnitude of the reverse current and higher symmetry of the current profile in the vicinity of $V = 0$ V upon annealing of the MoO₃ ABL. This is indicative of a lower barrier to hole transport to the anode and also an increase in the shunt currents that shows better carrier extraction and hence an improvement in overall conductivity.^{40,46} This higher extraction rate, therefore, results in the increase of the short-circuit current as was observed.

Numerical simulations by Wagenpfahl et al. show that the V_{oc} can depend on the charge extraction rate (S) at the electrode/organic interface (in this case, we examine only the MoO₃/organic interface, since the other interface is identical).^{51,52} Briefly, at open-circuit condition (where V_{oc} is measured), the electron extraction rate at the anode (S_n^a) has to be balanced by the hole extraction rate at the anode (S_p^a) since there is zero current in the device. A low hole extraction rate (S_p^a) is, therefore, balanced by hole accumulation at the interface for zero current. The accumulation of holes effectively shifts the hole quasi-Fermi level (E_{Fp}) toward the HOMO level, and this reduces the potential drop across the BHJ active layer.⁵² The slight improvements in V_{oc} observed in our devices can, therefore, be attributed to the reduction in hole accumulation. The higher extraction rate that reduces hole accumulation is also expected to reduce the interface recombination, and this is observed from the reduction in the value of R_p (assuming the same bulk and cathode interface recombination). Therefore, in summary, the improvements of the measured OPV parameters of J_{sc} , V_{oc} , R_s , and R_p are adequately explained by the increase in hole extraction rate at the MoO₃/organic interface brought about by the annealing process.

C. Understanding Origin of Extraction Rate Enhancement. Having showed that the improvements in the OPV devices are due to an enhancement in the hole extraction rates, its origin can be better understood through examining the electronic structure variations of MoO₃. Upon annealing, the filled defects are introduced as gap states together with reductions in the work function (WF) and ionization potential (IP). The latter results in a change in the energy alignment between the MoO₃ and the organic layers. This energy alignment before and after annealing is shown in Figure 3a,b,

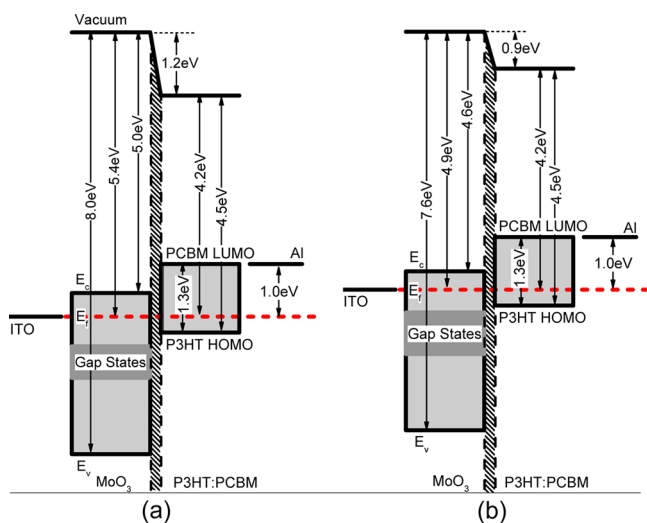


Figure 3. Energy alignments at the ITO/MoO₃/P3HT:PCBM interfaces for (a) as-deposited MoO₃ and (b) MoO₃ annealed at 250 °C. Details of the alignment are given in the text.

respectively. An Ohmic contact between the ITO and the MoO₃ is assumed, as was previously reported.⁵³ The Fermi level (E_F) and the valence level (E_v) position from the vacuum level of the MoO₃ layer was obtained from the WF and the IP as measured from the electron spectroscopy in this work. The defect states shown are also indicative of their relative energy level positions and bandwidths as obtained from the XPS spectra. The conduction band positions (E_c) were obtained from the band-gap measurements using UV-vis spectroscopy (Supporting Information, S4). The HOMO and LUMO positions of both the P3HT and the PCBM are taken from the literature values.^{54–57} The alignment at the MoO₃ and P3HT interface is obtained using the recent alignment model proposed by Greiner et al.⁵⁸ The universal model was derived after examining a series of metal oxide and organic semiconductor alignments, including MoO₃. In the model, when the WF of the metal oxide is higher than the IP of the organic semiconductor, the Fermi level of the metal oxide is pinned to 0.3 eV above the IP of the organic semiconductor. This finding is similar to predictions from the integer charge transfer model that is traditionally used to calculate the alignments at metal/organic interfaces.⁵⁹ In this work, as the WF of all the MoO₃ was measured to be larger than the P3HT IP, the MoO₃ Fermi level is effectively pinned at 0.3 eV above the P3HT HOMO level. It is critical that the work function of MoO₃ remains larger so that a favorable alignment is obtained, and this importance is also highlighted recently through the hydrogenation of MoO₃.⁴⁹ The energy level alignment in the active blend between P3HT HOMO and PCBM LUMO was estimated using the integer charge transfer (ICT) model.⁵⁴ The Al cathode Fermi level is taken to be aligned to the PCBM LUMO level.⁶⁰

First, from the electron spectroscopy data, we understand that the filled defect density is increased after the annealing. Second, these gap states now spread across a broader energy range for the annealed MoO₃, as shown schematically in Figure 3b. Finally, the resultant alignment between the defect states and the P3HT HOMO reduces after the annealing, and this makes hole injection from the P3HT into the gap states energetically more favorable. The increased in filled gap states density and range, together with a more favorable alignment of the defect states after annealing, can explain the increase in J_{sc} and the reduction in R_s . The entire transport process can be conceptualized by the injection of electrons from the ITO into the MoO₃, the extraction of holes from the P3HT into the MoO₃, and a recombination process.²⁰ Without the defects, the extraction of holes has to proceed via the deeper-lying valence band states. The creation of the defects, therefore, provided an additional pathway while an increase in the defect density enhances this hole extraction process. Our previous work that generated surface defects at the MoO₃/organic interface using sputtering also showed similar extraction improvements through an increase in J_{sc} .³⁸ This shows that bulk conductivity is not the key reason and the hole extraction rate at the anode interface (S_p^a) is critical. The increase of S_p^a will also help to reduce the hole accumulation at the interface and thus reduces the space charge buildup and improves the measured V_{oc} . The sharp improvements seen in the OPV device before and after annealing suggest that, in the absence of this additional pathway, the extraction process limits the overall OPV performance.

The alignment at the MoO₃/active layer interface in Figure 3a shows a vacuum discontinuity of 1.2 eV. Upon annealing,

this is reduced to 0.9 eV, as shown in Figure 3b. This change in alignment indicates that there is a change in the interface field after the annealing process. An attribution of this field drop to either interface dipoles or band bending is not trivial.^{59,61} However, we note that a lower interface field agrees with our earlier discussions on enhancement of extraction rate that reduces hole accumulation as this lowers the band bending at the interface. Further evidence of field reduction is present in the electron-blocking abilities of the interface between the organic layer and the MoO₃ ABL. The electron blocking at the MoO₃ ABL ability is postulated to be due to field effects, such as band bending, in a recent work.²⁰ The field reduction can, therefore, be observed from the forward biased dark current in Figure 2b that represents electron injection into MoO₃. The jump in the forward biased dark current at the intermediate annealing temperature can be explained by a poorer electron-blocking effect caused by reduction in field. Importantly, any field reduction at the interface is expected to reduce the mobility of carriers near the electrode/organic layer.⁶¹ This should, in turn, lower the hole extraction rate, which is contrary to what we observed. This shows that, in the context of this work, the defects play a more dominant role in hole extraction as compared to any field-enhancement effects. We, therefore, conclude that the improvement of the overall OPV device performance after annealing is brought about through defects-enhanced hole extraction. There is, however, a limit to the improvements brought about by the defects. As was discussed, the increase in defects is also countered by a reduction in the field at the interface that reduces the electron-blocking effect that increases recombination. This blocking effect is almost completely removed when MoO₃ becomes semimetallic at ~300 °C, and this explains the poor OPV performance observed for the device. In addition, the presence of excessive defects can actually reduce the optical transparency of the MoO₃ buffer layer, and this can similarly explain the saturation of J_{sc} at annealing temperatures of 200–250 °C.

4. CONCLUSION

This work investigates the role of defects and interface field for the MoO₃ anode buffer layers in an OPV device. A systematic increase in annealing temperature creates more defects and lowers the work function of the MoO₃. The defects provide an enhanced pathway for the hole extraction, and this can be observed from the different OPV device parameters, including the J_{sc} and V_{oc} . Although accompanied by a reduction in interface field, the defect-enhanced extraction dominates the overall OPV performance. The optimum annealing temperature is at 250 °C before the electron-blocking capability is affected by the presence of semimetallic MoO₂.

■ ASSOCIATED CONTENT

Supporting Information

Effect of buffer layer thickness, comparison of air-exposed and nonexposed OPV cells, evidence of nitrogen adsorption on MoO₃ surface, and MoO₃ band-gap measurements using UV–vis spectroscopy. This material is available free of charge via the Internet at <http://pubs.acs.org>.

■ AUTHOR INFORMATION

Corresponding Author

*Tel: 68745247 (S.Y.C.), 68744339 (J.Z.). Fax: 68748111. E-mail: chiamsy@imre.a-star.edu.sg (S.Y.C.), zhangj@imre.a-star.edu.sg (J.Z.).

Notes

The authors declare no competing financial interest.

■ REFERENCES

- (1) Krebs, F. C. *Sol. Energy Mater. Sol. Cells* **2009**, *93*, 394–412.
- (2) Manceau, M.; Angmo, D.; Jørgensen, M.; Krebs, F. C. *Org. Electron.* **2011**, *12*, S66–S74.
- (3) Krebs, F. C. *Sol. Energy Mater. Sol. Cells* **2009**, *93*, 1636–1641.
- (4) Krebs, F. C.; Tromholt, T.; Jørgensen, M. *Nanoscale* **2010**, *2*, 873–886.
- (5) Park, S. H.; Roy, A.; Beaupre, S.; Cho, S.; Coates, N.; Moon, J. S.; Moses, D.; Leclerc, M.; Lee, K.; Heeger, A. J. *Nat. Photonics* **2009**, *3*, 297–302.
- (6) Liang, Y.; Xu, Z.; Xia, J.; Tsai, S.-T.; Wu, Y.; Li, G.; Ray, C.; Yu, L. *Adv. Mater.* **2010**, *22*, E135–E138.
- (7) Po, R.; Carbonera, C.; Bernardia, A.; Camaioni, N. *Energy Environ. Sci.* **2011**, *4*, 285–310.
- (8) Steim, R.; Kogler, F. R.; Brabec, C. J. *J. Mater. Chem.* **2010**, *20*, 2499–2512.
- (9) Chen, L.-M.; Xu, Z.; Hong, Z.; Yang, Y. *J. Mater. Chem.* **2010**, *20*, 2575–2598.
- (10) Park, J. H.; Lee, T.-W.; Chin, B.-D.; Wang, D. H.; Park, O. O. *Macromol. Rapid Commun.* **2010**, *31*, 2095–2108.
- (11) Jørgensen, M.; Norrman, K.; Krebs, F. C. *Sol. Energy Mater. Sol. Cells* **2008**, *92*, 686–714.
- (12) Shrotriya, V.; Li, G.; Yao, Y.; Chu, C.-W.; Yang, Y. *Appl. Phys. Lett.* **2006**, *88*, 073508.
- (13) Ghasemi Varnamkhasti, M.; Fallah, H. R.; Mostajaboddavati, M.; Ghasemi, R.; Hassanzadeh, A. *Sol. Energy Mater. Sol. Cells* **2012**, *98*, 379–384.
- (14) Zilberberg, K.; Gharbi, H.; Behrendt, A.; Trost, S.; Riedl, T. *ACS Appl. Mater. Interfaces* **2012**, *4*, 1164–1168.
- (15) Subbiah, J.; Beaujuge, P. M.; Choudhury, K. R.; Ellinger, S.; Reynolds, J. R.; So, F. *Org. Electron.* **2010**, *11*, 955–958.
- (16) Kim, D. Y.; Subbiah, J.; Sarasqueta, G.; So, F.; Ding, H.; Irfan; Gao, Y. *Appl. Phys. Lett.* **2009**, *95*, 093304.
- (17) Liu, F.; Shao, S.; Guo, X.; Zhao, Y.; Xie, Z. *Sol. Energy Mater. Sol. Cells* **2010**, *94*, 842–845.
- (18) Kim, D. Y.; Sarasqueta, G.; So, F. *Sol. Energy Mater. Sol. Cells* **2009**, *93*, 1452–1456.
- (19) Murase, S.; Yang, Y. *Adv. Mater.* **2012**, *24*, 2459–2462.
- (20) Wong, K. H.; Ananthanarayanan, K.; Luther, J.; Balaya, P. J. *Phys. Chem. C* **2012**, *116*, 16346–16351.
- (21) Meyer, J.; Shu, A.; Kroger, M.; Kahn, A. *Appl. Phys. Lett.* **2010**, *96*, 133308–133303.
- (22) Irfan; Ding, H.; Gao, Y.; Small, C.; Kim, D. Y.; Subbiah, J.; So, F. *Appl. Phys. Lett.* **2010**, *96*, 243307–243303.
- (23) Greiner, M. T.; Chai, L.; Helander, M. G.; Tang, W.-M.; Lu, Z.-H. *Adv. Funct. Mater.* **2012**, *22*, 4557–4568.
- (24) Vasilopoulou, M.; Palilis, L. C.; Georgiadou, D. G.; Argitis, P.; Kennou, S.; Sygellou, L.; Kostis, I.; Papadimitropoulos, G.; Konofaos, N.; Iliadis, A. A.; Davazoglou, D. *Appl. Phys. Lett.* **2011**, *98*, 123301.
- (25) Kroger, M.; Hamwi, S.; Meyer, J.; Riedl, T.; Kowalsky, W.; Kahn, A. *Appl. Phys. Lett.* **2009**, *95*, 123301.
- (26) Wang, P.-S.; Wu, I.-W.; Tseng, W.-H.; Chen, M.-H.; Wu, C.-I. *Appl. Phys. Lett.* **2011**, *98*, 173302.
- (27) Buckley, A.; Pickup, D.; Yates, C.; Zhao, Y.; Lidzey, D. J. *Appl. Phys.* **2011**, *109*, 084509–084507.
- (28) Qi, X.; Li, N.; Forrest, S. R. *J. Appl. Phys.* **2010**, *107*, 014514–014518.
- (29) Bolink, H. J.; Coronado, E.; Orozco, J.; Sessolo, M. *Adv. Mater.* **2009**, *21*, 79–82.
- (30) Hancox, I.; Chauhan, K. V.; Sullivan, P.; Hatton, R. A.; Moshar, A.; Mulcahy, C. P. A.; Jones, T. S. *Energy Environ. Sci.* **2010**, *3*, 107–110.
- (31) Reynolds, K. J.; Barker, J. A.; Greenham, N. C.; Friend, R. H.; Frey, G. L. *J. Appl. Phys.* **2002**, *92*, 7556–7563.
- (32) Sun, Y.; Seo, J. H.; Takacs, C. J.; Seifert, J.; Heeger, A. J. *Adv. Mater.* **2011**, *23*, 1679–1683.

- (33) Meyer, J.; Kahn, A. *J. Photonics Energy* **2011**, *1*, 011109–011106.
- (34) Cho, S. W.; Piper, L. F. J.; DeMasi, A.; Preston, A. R. H.; Smith, K. E.; Chauhan, K. V.; Hatton, R. A.; Jones, T. S. *J. Phys. Chem. C* **2010**, *114*, 18252–18257.
- (35) Kanai, K.; Koizumi, K.; Ouchi, S.; Tsukamoto, Y.; Sakanoue, K.; Ouchi, Y.; Seki, K. *Org. Electron.* **2010**, *11*, 188–194.
- (36) Firment, L. E.; Ferretti, A.; Cohen, M. R.; Merrill, R. P. *Langmuir* **1985**, *1*, 166–169.
- (37) Werfel, F.; Minni, E. *J. Phys. C: Solid State Phys.* **1983**, *16*, 6091.
- (38) Chiam, S. Y.; Dasgupta, B.; Soler, D.; Leung, M. Y.; Liu, H.; Ooi, Z. E.; Wong, L. M.; Jiang, C. Y.; Chang, K. L.; Zhang, J. *Sol. Energy Mater. Sol. Cells* **2012**, *99*, 197–203.
- (39) Gao, J.; Perkins, C. L.; Luther, J. M.; Hanna, M. C.; Chen, H.-Y.; Semonin, O. E.; Nozik, A. J.; Ellingson, R. J.; Beard, M. C. *Nano Lett.* **2011**, *11*, 3263–3266.
- (40) Naguib, H. M.; Kelly, R. *J. Phys. Chem. Solids* **1972**, *33*, 1751–1759.
- (41) Miyata, N.; Suzuki, T.; Ohyama, R. *Thin Solid Films* **1996**, *281–282*, 218–222.
- (42) Chiam, S. Y.; Liu, Z. Q.; Pan, J. S.; Manipad, K. K.; Wong, L. M.; Chim, W. K. *Surf. Interface Anal.* **2012**, *44*, 1091–1095.
- (43) Choi, J.-G.; Thompson, L. T. *Appl. Surf. Sci.* **1996**, *93*, 143–149.
- (44) Greiner, M. T.; Helander, M. G.; Wang, Z. B.; Tang, W. M.; Qiu, J.; Lu, Z. H. *Appl. Phys. Lett.* **2010**, *96*, 213302.
- (45) Ramana, C. V.; Atuchin, V. V.; Pokrovsky, L. D.; Becker, U.; Julien, C. M. *J. Vac. Sci. Technol., A* **2007**, *25*, 1166–1171.
- (46) Bhosle, V.; Tiwari, A.; Narayan, J. *J. Appl. Phys.* **2005**, *97*, 083539.
- (47) Tokarz-Sobieraj, R.; Grybos, R.; Witko, M. *Appl. Catal., A* **2011**, *391*, 137.
- (48) Scanlon, D. O.; Watson, G. W.; Payne, D. J.; Atkinson, G. R.; Egde, R. G.; Law, D. S. L. *J. Phys. Chem. C* **2010**, *114*, 4636–4645.
- (49) Vasilopoulou, M.; Douvas, A. M.; Georgiadou, D. G.; Palilis, L. C.; Kennou, S.; Sygellou, L.; Soultati, A.; Kostis, I.; Papadimitropoulos, G.; Davazoglou, D.; Argitis, P. *J. Am. Chem. Soc.* **2012**, *134*, 16178–16187.
- (50) Dang, M. T.; Hirsch, L.; Wantz, G. *Adv. Mater.* **2011**, *23*, 3597–3602.
- (51) Wagenpfahl, A.; Deibel, C.; Dyakonov, V. *IEEE J. Sel. Top. Quantum Electron.* **2010**, *16*, 1759–1763.
- (52) Wagenpfahl, A.; Rauh, D.; Binder, M.; Deibel, C.; Dyakonov, V. *Phys. Rev. B: Condens. Matter Mater. Phys.* **2010**, *82*, 115306.
- (53) Vasilopoulou, M.; Palilis, L. C.; Georgiadou, D. G.; Kennou, S.; Kostis, I.; Davazoglou, D.; Argitis, P. *Appl. Phys. Lett.* **2012**, *100*, 013311–013314.
- (54) Xu, Z.; Chen, L.-M.; Chen, M.-H.; Li, G.; Yang, Y. *Appl. Phys. Lett.* **2009**, *95*, 013301–013303.
- (55) Wei, H.; Scudiero, L.; Eilers, H. *Appl. Surf. Sci.* **2009**, *255*, 8593–8597.
- (56) Tengstedt, C.; Osikowicz, W.; Salaneck, W. R.; Parker, I. D.; Hsu, C.-H.; Fahlman, M. *Appl. Phys. Lett.* **2006**, *88*, 053502–053503.
- (57) Brabec, C.; Dyakonov, V.; Scherf, U., Eds. *Organic Photovoltaics: Materials, Device Physics, and Manufacturing Technologies*; Wiley-VCH: Weinheim, Germany, 2008.
- (58) Greiner, M. T.; Helander, M. G.; Tang, W.-M.; Wang, Z.-B.; Qiu, J.; Lu, Z.-H. *Nat. Mater.* **2012**, *11*, 76–81.
- (59) Braun, S.; Salaneck, W. R.; Fahlman, M. *Adv. Mater.* **2009**, *21*, 1450–1472.
- (60) Frohne, H.; Shaheen, S. E.; Brabec, C. J.; Müller, D. C.; Sariciftci, N. S.; Meerholz, K. *ChemPhysChem* **2002**, *3*, 795–799.
- (61) Lange, I.; Blakesley, J. C.; Frisch, J.; Vollmer, A.; Koch, N.; Neher, D. *Phys. Rev. Lett.* **2011**, *106*, 216402.